Materialia 18 (2021) 101155

Contents lists available at ScienceDirect

Materialia

journal homepage: www.elsevier.com/locate/mtla

Full Length Article

Temperature-induced structural phase transformation in samples of Co_3O_4 and $Co_{3-x}Ni_xO_4$ for CoO

L.J. Cardenas-Flechas[a], P.T.C. Freire[b], E.C. Paris[c], L.C. Moreno[d], M.R. Joya[e,*]

[a] Departamento de Ingeniería Mecánica y Mecatrónica, Universidad Nacional de Colombia, Bogotá, C.P. 111321, Calle 45 #30-03, Colombia
[b] Departamento de Física, Universidade Federal do Ceará, P.O. Box 6030, Fortaleza, CE, 60455-900, Brazil
[c] Nanotechnology National Laboratory for Agriculture (LNNA), Embrapa Instrumentação, XV de Novembro St., 1452, 13560-970 São Carlos, SP, Brazil
[d] Departamento de Química, Universidad Nacional de Colombia, Bogotá, C.P. 111321, Calle 45 #30-03, Colombia
[e] Departamento de Física, Universidad Nacional de Colombia, Bogotá, C.P. 111321, Calle 45 #30-03, Colombia

ARTICLE INFO

Keywords:
Co_3O_4
Nickel
Hydrothermal
Temperature
Structural phase transformation

ABSTRACT

Undoped and Ni-doped cobalt oxide (Ni=4%) powders were prepared by hydrothermal synthesis and subsequently examined. The powders obtained were subjected to thermal annealing at temperatures ranging between 600 °C and 1000 °C. The experimental results indicate that the annealing affects the structural properties with the phase change Co_3O_4 to CoO. X-Ray diffraction (XRD) analysis reveals the presence of pure spinel phase up to 800 °C in powders obtained with and without the addition of nickel. From 900 °C, the CoO phase was observed. Rietveld refinement was conducted with main GOF values between 1.09 and 1.26 and also x_2 values between 1.28 and 1.57, indicating a good correspondence between the simulated and the experimental pattern. In addition, SEM measurements evidenced that particle size increased with temperature; however, samples doped with Ni exhibited a slightly smaller size compared to pure samples. The synthesized powders showed shifted and broad bands Raman, with increasing temperature, mainly for doped samples. These changes in the position of Raman vibrational modes are related to defects and distortions in the crystal lattice of the material as a result of the increase in temperature and the addition of Ni. Furthermore, such changes may also indicate loss of crystallinity in the material, or the beginning of the phase change.

1. Introduction

In recent decades, several efforts have been made to improve the electrical, catalytic, among other characteristics of different materials. Among the main studies on the subject, many have studied the variation and changes in the methods of sample preparation in order to change the morphology and doping of the samples to improve the physical, chemical and structural properties of such materials [1]. Cobalt oxide (Co_3O_4) has a spinel structure with remarkable electrical and chemical properties. This explains why several studies have been carried out to study its composition as well as different one to prepare it, since its atoms have shown efficient and stable activity in different alkaline media [1, 2-4]. Some of the properties of cobalt tetroxide include high detection response, simple electronic measurement and compatibility, supercapacitor, water division, excellent catalytic and electrochemical properties, as well as interesting magnetic and optical properties with applicability in electronic devices [5-7]. Methods for obtaining Co_3O_4 and its compounds include the deposition-precipitation method [8], sonochemical synthesis [9], electrophoretic deposition - thermal and hydrothermal reduction [10], complete green process [11], solid state reaction [12], and microwaving assistance. Some of these methods allow for efficient electron transmission and high structural stability of the material.

According to Zhou et al., [13] the general strategy of isovalent replacement is a new opportunity to improve the catalytic activity of transition metal oxides, such as cobalt oxide. At the same time, several doping preparations use metal ions like Li, Fe and Cu to dope cobalt oxide, improving its properties [14]. Replacing cobalt with a high concentration of iron in the perovskite structure improves electrocatalytic activity [15]. Polycrystalline nanowires substituted with Cu- Co_3O_4- Cu exhibit much greater catalytic activity than those with pure Co_3O_4 polycrystalline nanowires [13]. Co_3O_4 doped with graphene showed an increase in power, energy, and specific area [16]. Most applications are focused on the use of particles with high specific surface areas and nano-sized particles [17].

The analysis of Ni-Co_3O_4 synthesis can be decisive for catalytic activities, since factors such as chemical composition, elemental valence, crystal structure and surface state can directly influence catalysis [18]. Li et al., [1] performed the synthesis of porous Co_3O_4 nanoplates doped with different percentages of nickel to determine the improvement of

* Corresponding author.
E-mail address: mrinconj@unal.edu.co (M.R. Joya).

https://doi.org/10.1016/j.mtla.2021.101155
Received 25 March 2021; Accepted 24 June 2021
Available online 29 June 2021

reaction activity in the evolution of oxygen and hydrogen. Gao et al., [19] synthesized Co_3O_4 in nickel foam with promising results for non-metallic catalysts in reducing nitrate. Kozlovskiy et al., [20] performed FeCo–Fe_2CoO_4 / Co_3O_4 annealing in some samples where they found that the ordering and formation of oxide phases with predominance of Fe_2CoO_4 phase generates a minimization in the distortions of the crystal structure. In turn, Zdorovets et al., [21] analyzed changes in the phase composition of Co nanowires where a change in magnetic properties and an increase in conductivity were observed up to a temperature of 600 ˚C.

Nickel doping on Co_3O_4 is a viable alternative since Ni is in the same period as cobalt and its ionic radius is similar, therefore Ni ions can serve as electron donors for Co_3O_4. [22], Additionally, the transition metal Ni possesses a stable chemical bonding force with intermediates due to its unique 3D electronic structures [23], in addition to improved electrical conductivity. Ni-doped porous Co_3O_4 nanostructures also provide a high number of active sites exposed to surface reactions [24]. Doping can influence the crystal structure, grain size, and oxygen distribution of a compound that can be beneficial in different types of applications [25]. Through phase transition analysis and mechanisms, it is possible to understand structural properties under different conditions including temperature, pressure, doping in order to find new structural models [26]. Thus, it is necessary to continue investigating on the electrical, magnetic and morphological properties of this material, as well as its specific characteristics involved in structural phase transitions.

In this work, pure Co_3O_4 and Ni-Co_3O_4 were synthesized by hydrothermal technique and subsequently calcined at 600, 700,750,800, 900, and 1000 ˚C to examine the structural phase transition in the samples with increasing calcination temperature. To the best of our knowledge, there is no detailed study in the literature on the phase transition of nickel cobalt oxide with increasing calcination temperatures. The samples obtained were characterized by different techniques, such as X-ray diffraction (XRD), energy dispersion spectroscopy (EDS), Raman spectroscopy, and scanning electron microscopy (SEM). This study evidenced that the studied samples do not have secondary phases up to 800 ˚C, as well as showing that the Ni ions were incorporated into the Co_3O_4 lattice. Therefore, the spinel structural phase transition was observed in the samples of pure Co_3O_4, while with the addition of 4% Ni and the increase in temperatur, the CoO phase was only evident at 900 ˚C.

2. Material and methods

2.1. Preparation of Co_3O_4

A sample of 1.926 g of cobalt acetate ($Co(C_2H_3O_2)_2$•$4H_2O$, Synth, PM = 249.08 g/mol) was dissolved in 80 ml distilled water (concentration = 0.1 M). When the cobalt precursor was completely solubilized, 0.96 g of urea (CH_4N_2O, Vetec, PM= 60.06 g / mol) was added and 2 ml of ammonia (NH_4OH, LS Chemicals, PM = 35.05 g / mol) were added dropwise to adjust the pH to 9.2 and then stirred at room temperature for 1 h. The homogeneous solution was transferred to a Teflon lined autoclave (120 ml), which was hermetically sealed and heated at 180 ˚C for 20 h (3 ˚C/ min). After cooling the sample to room temperature, the precipitates were collected and washed twice with distilled water (pH = 7), rinsed with ethanol and dried in an oven at 60 ˚C for 7 h. Finally, the powders obtained were calcined in air at 300 ˚C for 3 h (10 ˚C/min).

2.2. Preparation of Co_3O_4 / Ni (4%)

A sample of 1.9129 g of cobalt acetate ($Co(C_2H_3O_2)_2$ * $4H_2O$, Synth, PM = 249.08 g / mol) was dissolved in 80 ml of distilled water (concentration = 0.1 M). When the cobalt precursor was completely solubilized, 0.0841 g of nickel sulfate ($NiSO_4$ • $6H_2O$, synthesizer, PM = 262.85 g / mol) was added. With dissolved metal precursors, 0.96 g of urea (CH_4N_2O, Vetec, PM = 60.06 g / mol) was added and 2 ml of ammonia (NH_4OH, LS Chemicals, PM = 35.05 g / mol) were added dropwise to adjust the pH to 9.2, and then stirred at room temperature for 1 h. The homogeneous solution was transferred to a Teflon-coated autoclave (120 ml), which was hermetically sealed and heated at 180 ˚C for 20 h (3 ˚C/min). After cooling the sample to room temperature, the precipitates were collected and washed four times with distilled water (pH = 7), rinsed with ethanol and dried in an oven at 60 ˚C for 7 h. Finally, the powders obtained were calcined in air at 300 ˚C for 3 h (10 ˚C/ min). Fig. 1 shows the process of obtaining the samples.

3. Results and discussion

Fig. 2 shows the XRD powder patterns of (a) Co_3O_4 and (b) $Co_{3-x}Ni_xO_4$ (x = 0.04) synthesized by the hydrothermal method and subsequently calcined at 600, 700, 750 and 800 ˚C for a time interval of 2 h. In Fig. 2(a), the diffractograms of cobalt oxide in the spinel phase and the formation of the crystalline phase of Co_3O_4 with variation in peak intensity are observed. In Fig. 2(b) the cobalt oxide Co_3O_4 was modified with the addition of 4% Nickel and subsequently calcined at the temperatures mentioned above. The XRD peaks in the Ni samples were also allocated to the cubic spinel phase of Co_3O_4. No secondary phase of nickel oxide was observed.

All powders obtained (up to 800 ˚C) exhibited diffraction peaks compatible with the cubic spinel structure of the Co_3O_4 space group *F-43 m* as provided in Cod.00–001–1152 file simultaneously in accordance with other researches [27,28]. The X-ray diffraction pattern with reflection peaks is associated with the planes (220), (311), (222), (400), (422), (511) and (440) at 2θ = 31.26˚, 36.85˚, 38.63˚, 44.81˚, 55.79˚, 59.42˚ and 65.36˚, respectively. The preferential direction and orientation (311) were also considered. With the increase in temperature, an improvement in the peak intensity was observed. Such a change can be attributed to the increased crystallinity in the samples [29, 30]. According to other investigations [31], there is a great similarity between the crystalline phase of Ni-doped Co_3O_4 and the cubic spinel phase of Co_3O_4 when there is no phase transition, which is a consequence of nickel atoms being housed in the matrix of the cobalt oxide lattice by means of a "substitution". This work reports that the modification of nickel at 4% does not cause significant effects on the structural modification of the samples calcined at different temperatures when compared with pure counterpart samples.

Fig. 3 shows the regular Co_3O_4 crystal spinel structure where the Co^{3+} ions are in the octahedral interstices and the Co^{2+} ions are in the tetrahedron of the cubic lattice of cobalt oxide (II. III) [32]. In the ideal cobalt tetraoxide structure, there is a single unit cell and 8 elementary units where half of the octahedral sites are occupied by trivalent cations and an eighth of the available tetrahedral sites are occupied by divalent cations. Co_3O_4 is an oxide with an AB_2O_4 spinel structure where the tetrahedral sites A with Co^{2+} (d^7) cations and the middle octahedral sites B fit to the Co^{3+} (d^6) cations. This ideal occupation is affected by high calcination temperatures leading to oxygen vacancies. The formation of oxygen vacancies involves the reduction of octahedral trivalent cobalt and is accompanied by the migration of divalent tetrahedral cobalt to empty interstitial octahedral positions [32-34]. The division of 3d levels causes Co^{3+} ions located in the octahedron to have a diamagnetic behavior, as well as the total filling of the t_{2g} levels that do not favor the net magnetization resulting from vacancies in the octahedral sites [35].

Table 1 shows the EDS analysis with percentages of atomic concentration of the chemical elements in the study samples. The samples of pure Co_3O_4 and 4% Ni- Co_3O_4 that were heat treated from 600 ˚C to 800 ˚C with elements such as Co, C and Ni are listed in Table 1. A variation in the atomic percentage is observed as a function of the calcination temperature, as well as the addition of the nickel percentage. For Co_3O_4 at 600 ˚C, the percentage of cobalt is evident at 65.44% increasing 4.92% when exposed to 700 ˚C; finally, the atomic percentage reached 72.32% at 800 ˚C. The addition of nickel percentage is = 4% which is evident in

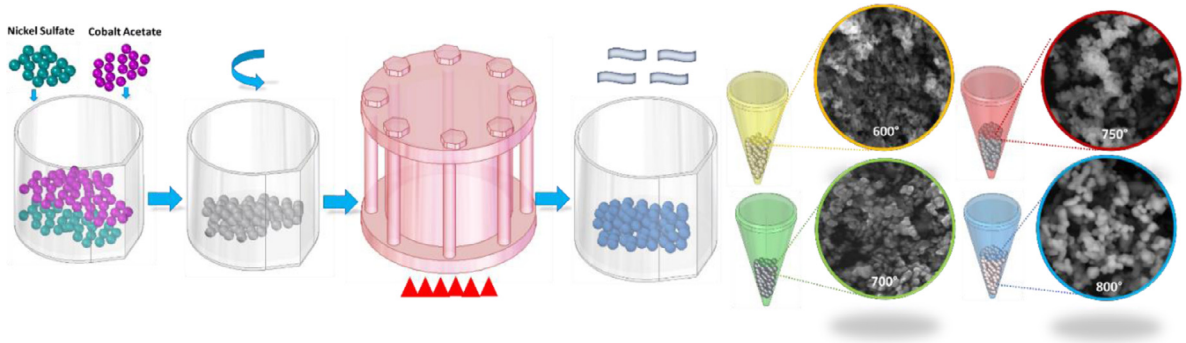

Fig. 1.. Schematic illustration of the Co_3O_4 – $Co_{3-x}Ni_xO_4$ preparation process.

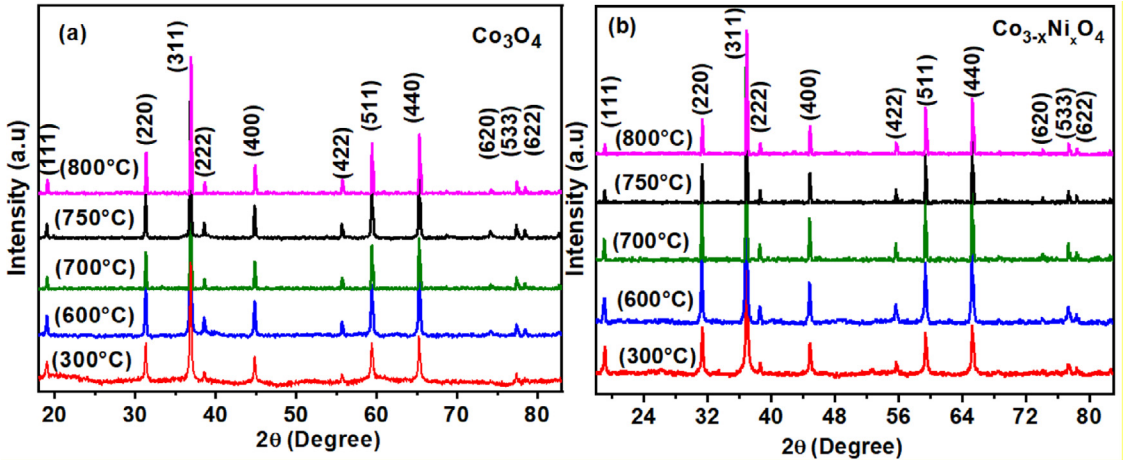

Fig. 2. X-ray spectra (XRD) for Co_3O_4 samples obtained via hydrothermal technique: (a) Co_3O_4 (b) $Co_{3-x}Ni_xO_4$ calcined at 600,700, 750, 800 °C respectively from bottom to top.

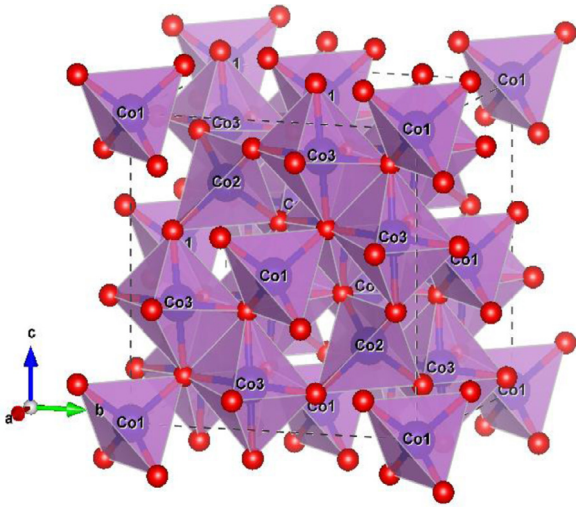

Fig. 3. Structural Co_3O_4 arrangement in the spatial group *F –43 m.*

the results of the $Co_{3-x}Ni_xO_4$ samples with a very low percentage that increases from 1.15% at 600 °C to 1.54% at 800 °C. The presence of a carbon peak is attributed to the carbon tape used as the sample support in the analysis. These results can be associated with those obtained by Koli et al., [36] where cobalt oxide and doped nanoparticles are associated with the composition of particular components of the synthesis.

Table 1
Chemical composition of Co_3O_4 - $Co_{3-x}Ni_xO_4$, x = 4% nickel-doped samples.

	600 °C		700 °C		800 °C	
	Elem.	% at	Elem.	% at	Elem.	% at
Co_3O_4	Co K	65.44	Co K	70.36	Co K	72.32
	C K	9.64	C K	7.91	C K	5.65
$Co_{3-x}Ni_xO_4$	Co K	67.72	Co K	69.51	Co K	71.25
x = 4%	C K	4.81	C K	8.18	C K	7.25
	Ni K	1.15	Ni K	1.16	Ni K	1.54

Fig. 4(b) shows the nickel substitution at Co_3O_4 $^{2+}$ and $^{3+}$sites. The characteristics of Co_3O_4 can be improved in several ways, including replacing the $^{2+}$ sites in other divalent cations [14]. Ni^{2+} is a good candidate to replace Co^{2+} and Co^{3+} in the cobalt spinel lattice (II, III), since it has a similar ionic radius, especially with the $^{2+}$ cation charge. In addition, the change in the surrounding Co-binding environment can affect the intrinsic activity of Co^{3+} and the replacement of Co^{2+} by Ni^{2+}. In relation to previous studies, the replacement of Ni^{2+} in the spinel structure of Co_3O_4 causes the material to have higher electrical conductivity, which may be associated with the interaction between the effective mass and the band gap of the given material [37]. Impurity band type conduction is induced due to lower quantity of divalent nickel. Therefore, electrons can move from an occupied (Ni^{2+}) to an empty (Ni^{3+}) site. In Fig. 4(b), modifications are observed in the structure of the cobalt spinel with Sb [38], Fe [39], Si [40], V and Ge. Synthetic spinel phase of Co_2SiO_4 was studied to determine the effect of pressure on the lattice parameters with values of 8.139 Å at 23 °C [41]. In addition, a correlation was established between stability of the structural phase

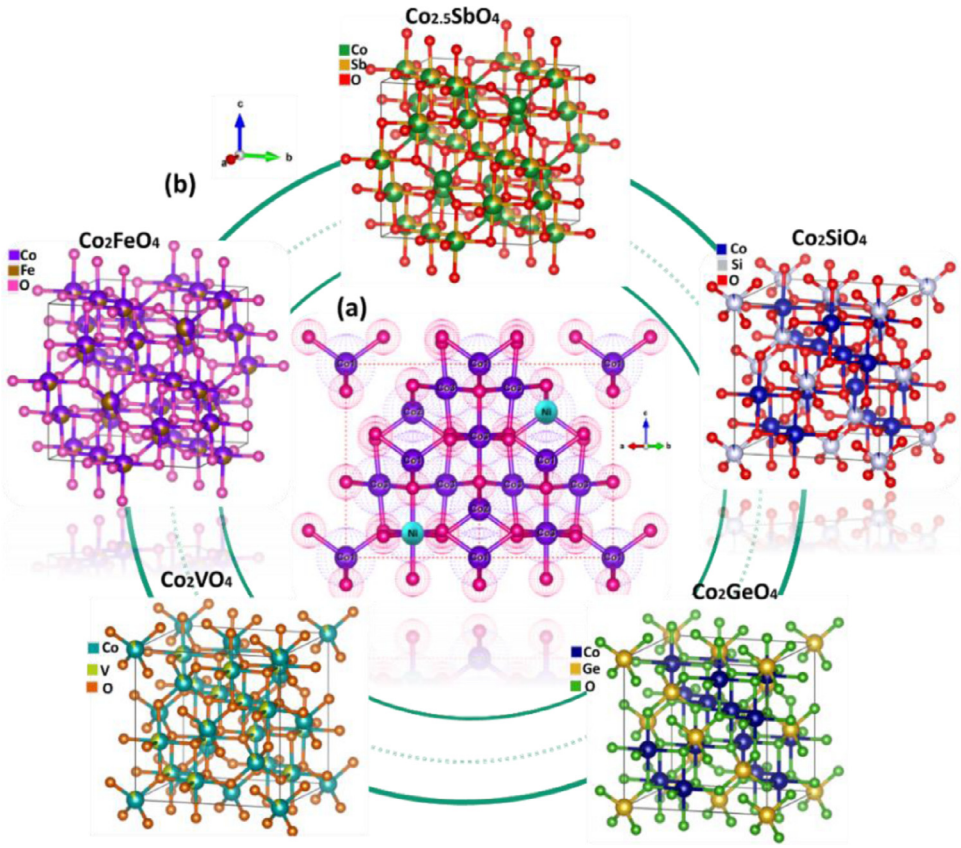

Fig. 4. (a) Co_3O_4 structure at the *F-43 m* spatial group with nickel substitution at $^{2+}$ (right) and $^{3+}$ (left) sites. (b) Other cobalt-based elements found in the literature (Table 2).

Table 2
Some cobalt-based spinel compounds and their characteristics.

Compound	Obtention method	Characteristics	Refs
Co_2SiO_4	Floating zone method	Crystal culture of cobalt silicate Displacement densities in the order of 10^5–10^6 cm^{-2} Crystals of 30–60 mm long and 6–10 mm in diameter.	[44, 45]
Co_2VO_4	Cation exchange method	Marrying metallic vanadium atomic chains with electroactive cobalt cations. Superior performance attributed to its unique electronic configuration, where the octahedrally coordinated Co^{2+} cations take the LS state with an ideal electron occupation (E_{g1}).	[43]
Co_2FeO_4	Mechanical alloy and annealed	Co_2FeO_4 has a ferrimagnetic character independent of the stability of the structural phase. A coexistence of two ferromagnetic phases was found, except at 900 °C. At iron lattice positions under different temperatures, cobalt atoms diffuse unevenly.	[42] [46]
Co_2GeO_4	Hydrothermal flow synthesis	Specific capacity of 240 mAh g^{-1}. Average particle size of 17 ± 5 nm. Variety of especially spherical or cubic morphologies. The compound exhibits poor performance based on scanning speed tests.	[47]
Co_2CuO_4	Solvothermal method	Increased catalytic activity towards peroxymonosulfate (PMS) activation due to the presence of "Co^{2+}" on the catalyst surface and the combined catalytic reactivity of copper and cobalt.	[48]
Co_2ZnO_4	Low temperature aqueous processing route	Depending on the calorimetric behavior, the compound indicates changes in the pin state with temperature and composition. Enthalpy values of the mixture that exceed previously recorded values.	[49]
Co_2LiO_4	Sol-gel method assisted with poly-acrylic acid (PAA)	Paramagnetic behavior without indication of magnetic ordering up to 5 K. Formation of a metastable spinel phase in the lattice.	[50]
Co_2MnO_4	Deposition / precipitation in situ	The inclusion of palladium in the spinel structure visibly improves the reducibility of the catalysts, in addition to achieving better stability of the catalytic cycle performance in the oxidation of methane for Co_2MnO_4.	[51]
Co_2NiO_4	Physical vapor deposition	A high conductivity of up to 204S/cm was observed in thin films of Co_2NiO_4, as well as potential applications in optoelectronic devices.	[52]

and the magnetic properties of Co_2FeO_4 exhibiting a particle size of 25 to 45 nm [42]. In Co_2VO_4, electroactive cobalt cations were bound to atomic chains of vanadium, where the Co^{2+} cations in the octahedral sites assumed the low spin state [43]. Table 2 shows some additional cobalt-based spinel compounds, production methods, and their respective characteristics mentioned in the available literature.

The Rietveld refinement was performed with the data obtained experimentally using the General Structure Analysis System-II (GSAS-II) as shown in Fig. 5. Fig. 5(a) presents the experimental and calculated pattern of Co_3O_4 calcined at 600 °C. Fig. 5(b) presents XRD $Co_{3-x}Ni_xO_4$ (= 4%) patterns calcined at the same temperature. Fig. 5(c) and 5(d), respectively, show the experimental and calculated XRD patterns for

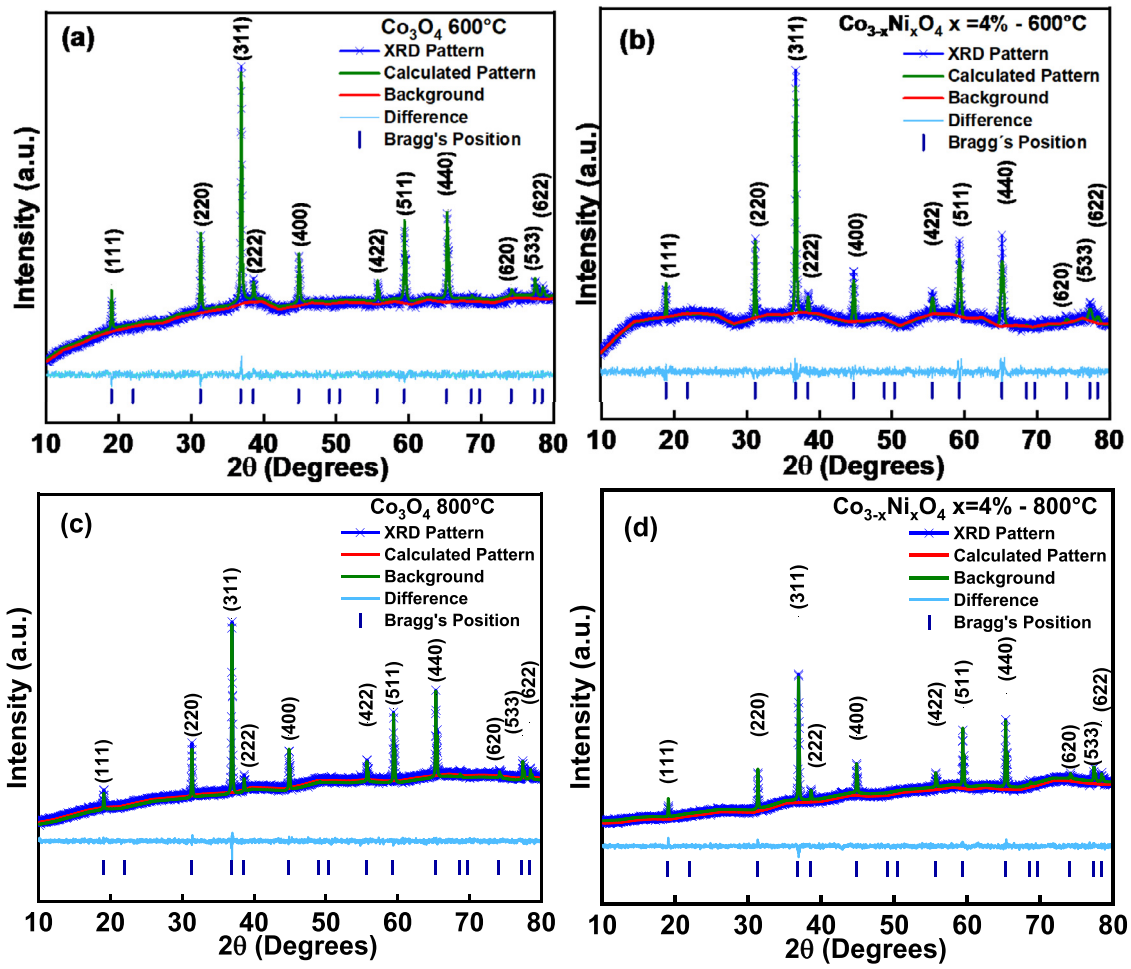

Fig. 5. XRD refined pattern for (a) Co_3O_4 600 °C (b) $Co_{3-x}Ni_xO_4$ x = 4%, 600 °C (c) Co_3O_4 800 °C (d) $Co_{3-x}Ni_xO_4$ x = 4%, 800 °C. The blue symbols represent the experimental diffraction data. Calculated patterns are represented by the base line. The vertical line is Bragg's. The lower trace depicts the difference between the experimental and calculated intensity values.

Table 3
Lattice parameters Co_3O_4.

Temperature (°C) Co_3O_4	$a = b = c$ (Å)	$\alpha=\beta=\gamma$	Vol(Å^3)
600	8.08194	90 °C	527.895
700	8.08420	90 °C	528.336
750	8.08448	90 °C	528.392
800	8.08551	90 °C	528.593
$Co_{3-x}Ni_xO_4$, x = 4%			
600	8.08576	90 °C	528.643
700	8.08762	90 °C	529.008
750	8.08827	90 °C	529.136
800	8.09176	90 °C	529.820

Table 4
Positions Co_3O_4.

Co_3O_4 Positions			
	x	y	Z
Co_1	0.0000	0.0000	0.0000
Co_2	0.2500	0.2500	0.2500
Co_3	0.6250	0.6250	0.6250
O_1	0.3900	0.3900	0.3900
O_2	0.1400	0.1400	0.1400

Co_3O_4 and $Co_{3-x}Ni_xO_4$ = 4% for samples calcined up to 800 °C. The refinement contributed to determine that Co_3O_4 crystallizes in a spinel structure in an *F-43 m* space group.

The lattice parameters and the volume of the unit cell are shown in Table 3, where the addition of nickel results in a higher lattice parameter compared to the undoped samples. In addition, it exhibits an increase in the volume of the unit cell in the crystal lattice. For this study, the cubic spinel structure remains stable in the 600 to 800 °C temperature range. The parameters $a = b = c$ show an increase as the temperature increases for Co_3O_4 in 8.08551 Å, and $Co_{3-x}Ni_xO_4$ in 8.09276 Å at a temperature of 800 °C. An increase in volume and unit cell was also observed with an average value of 528,304 Å for Co_3O_4 and 529.15 Å for the nickel-doped sample. According to the data obtained in the refinement, the Co_3O_4 positions on the x, y, z of Co_1, Co_2, Co_3, O_1 and O_2 are shown in Table 4. These results may be associated with cationic disorder at the tetrahedral and octahedral sites of the Co_3O_4 rotation structure.

As the calcination temperature increases in the samples, for both the pure Co_3O_4 and for the Ni-added sample, there is a distortion in the crystal lattice. Samples at lower temperatures evidence high crystallinity, where there is an improvement in the free energy state of the crystals, causing an increase in the constant lattice, an expansion of the lattice, as well as a change in the lattice parameter [53]. However, as the calcination temperature increases, a structural phase change occurs. According to Du et al., 2020 the effect of nickel doping in the Co_3O_4 arrays produces a better activity in the oxygen evolution reaction asso-

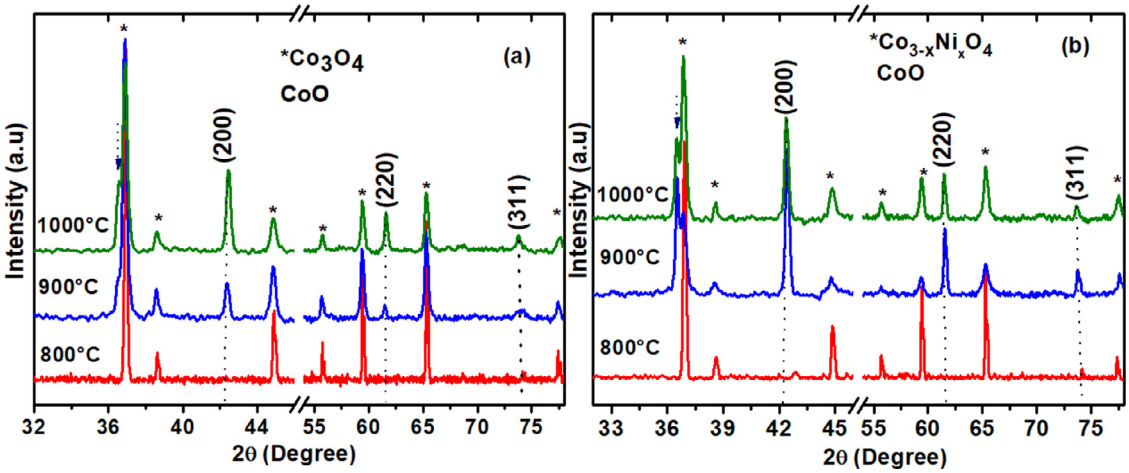

Fig. 6. X-ray spectra (XRD) for the Co_3O_4 samples obtained via hydrothermal technique. (a) Co_3O_4. (b) $Co_{3-x}Ni_xO_4$. From bottom to top, respectively calcined at 750, 800, 900, and 1000 ˚C.

Table 5
Refinement parameters.

Refinement parameters Co_3O_4						
Temperature (˚C)	X^2	R_{esp}	R_E	R(BS)	Rwp (BS)	GOF
600	1.18	1.08%	0.91%	1.41%	1.17%	1.09
700	1.30	1.20%	1.05%	1.78%	1.36%	1.14
750	1.27	1.22%	1.06%	1.78%	1.37%	1.13
800	1.16	1.20%	1.22%	1.92%	1.92%	1.08
Refinement parameters $Co_{3-x}Ni_xO_4$ x = 4% – 600 ˚C						
	X^2	R_{esp}	R_E	R(BS)	Rwp (BS)	GOF
600	1.58	1.06%	0.99%	1.92%	1.33%	1.26
700	1.25	1.10%	0.96%	1.63%	1.22%	1.12
750	1.16	1.30%	1.09%	1.66%	1.39%	1.08
800	1.30	1.35%	1.17%	1.97%	1.53%	1.14

ciated with the synergistic effects that are generated between cobalt and nickel as well as the modification of its atomic structure. [54].

High performance Co-based microwave absorbers with a unique structure and characteristics can be designed apart from the evolution of morphology and the phase of CoO/Co3O4 [55]

Details on the high-temperature crystal structure of Co_3O_4 are still poorly understood and remain an area of active research. Specifically, in relation to the sudden non-linear increase in the lattice parameter that indicates a structural abnormality at high temperature. Depending on the temperature ranges used, the insertion of a dopant plays an important role in increasing conductivity, as well as in the evolution of activation energy [56]. The values of the main Rietveld refinement parameters are presented in Table 5. The results indicate a high quality of refinement for the temperature range between 600 and 800 ˚C: x^2:1.16 and 1.32 Rwp: 1.18 and 1.20 on average, for Co_3O_4 and doped samples, respectively, where there is a good correspondence between the simulated and the experimental patterns.

Fig. 6 shows the diffractograms for (a) Co_3O_4 and (b) $Co_{3-x}Ni_xO_4$ of the XRD pattern obtained at 750, 800, 900 and 1000 ˚C. At 900 ˚C, peaks located at 36.4˚ are observed. Likewise, peaks at 42.3˚, 61.4˚ and 73.6˚ are observed for the CoO-FCC characteristics that correspond to the planes (111) (200) (220) and (311) indexed in the crystal chart JCPDS No. 43–1004. These results indicate that the transformation of the Co_3O_4 phase generated by calcination temperature occurs at 900 ˚C-1000 ˚C. At temperatures above 850 ˚C, there is a change in Gibbs free energy.

This value is negative and is associated with the formation of the CoO phase at high temperature [57,58]. According to Shobaky et al., [59] reticular expansion, as well as increasing particle size, is a trend in the synthesis of Co_3O_4 nanoparticles by different methods. Doping, in turn, generates changes in the order of the phases of Co_3O_4 at different temperatures [60]. As seen in Fig. 6(b) for cobalt oxide doped with 4% Ni, the structural phase transition at 900 ˚C also occurs. However, at 800 ˚C, a small shoulder at approximately 43 (2θ) can be seen in Fig. 6(b). This may be indicative of the effect of nickel on the crystal lattice of the cobalt oxide spinel phase. In this sense, the increase in energy in the structural lattice of the samples, both for the pure and for doped with Ni, makes them move to a more stable and simple phase like that of CoO.

Co_3O_4 and $Co_{3-X}Ni_XO_4$,= 4% Ni crystallite size from 600 ˚C to 1000 ˚C is shown in Table 6. The peak indexed as (311) was used to establish the value by means of the Scherrer equation. All samples indicated a crystallite size of approximately 25–80 nm. In addition, with the increase in the calcination temperature, an increase was observed where the highest temperature reached 800 ˚C. However, from 900 ˚C onwards, the crystallite size decreased to 26.86 for the Ni-added sample exposed to 1000 ˚C. This decrease in the size of the crystallite indicates loss of crystallinity caused by vacancies of oxygen and cobalt, which explains the peaks in the CoO phase. The increase in the size of the crystallite in metal oxides can be achieved with a progressive increase in temperature in the calcination process. It should be noted, however, that the final heat treatment affects the morphology of metal oxides, increasing size of the particle [61]. Thus, some characteristics of the samples may vary considering the agglomerations generated by the crystallites. These can be seen in terms of the size and shape of the nanoparticles in the SEM measurements. The results presented in Table 6 showed notably that the addition of nickel favors the decrease in crystallite growth by increasing the temperature in relation to the crystallite growth in pure samples.

Fig. 7(a) shows the Raman spectra of the Co_3O_4 samples and (b) of the $Co_{3-x}Ni_xO_4$ with = 4% at the following calcination temperatures: 600 ˚C, 700˚, 750˚ and 800 ˚C, with the five active Raman modes ($A_{1g} + E_g + 3F_{2g}$) corresponding to the Co_3O_4 phase in the spinel structure [62]. The five bands are found at approximately 196, 482, 521, 618, 687cm^{-1}, shown in Fig. 7. The A_{1g} mode located at 687 cm^{-1} is associated with the symmetric stretching vibration of Co^{3+}- O (CoO_6 octahedral sites). The bands located at 196, 520, 617 cm^{-1} correspond to the F_{2g} mode, while the band located at 196 cm^{-1} is attributed to the characteristic vibrations of the tetrahedral sites (CoO_4). Depending on the calcination temperature, slight displacements are observed, as well as variation in the shape of the peaks. These variations are probably associated with structural defects or vacancies of cobalt and oxygen in the samples. This variation is probably associated with structural defects or vacancies of cobalt and oxygen in the samples. Nevertheless, as they are

Table 6
Crystallite size calculation using the Debye Scherrer equation.

Sample	Peak position (2θ)	FWHM (degree)	Crystallite size (nm)
Co_3O_4 – 600 °C	36.877	0.234	35.773
Co_3O_4 – 700 °C	36.899	0.192	43.601
Co_3O_4 – 800 °C	36.914	0.105	79.732
Co_3O_4 – 900 °C	36.843	0.265	31.585
Co_3O_4 – 1000 °C	36.877	0.280	29.896
$Co_{3-x}Ni_xO_4$, x = 4% – 600 °C	36.845	0.267	31.349
$Co_{3-x}Ni_xO_4$ x = 4%– 700 °C	36.849	0.200	41.851
$Co_{3-x}Ni_xO_4$ x = 4%- 800 °C	36.890	0.109	76.800
$Co_{3-x}Ni_xO_4$ x = 4%– 900 °C	36.811	0.300	27.898
$Co_{3-x}Ni_xO_4$ x = 4%– 1000 °C	36.816	0.2948	26,860

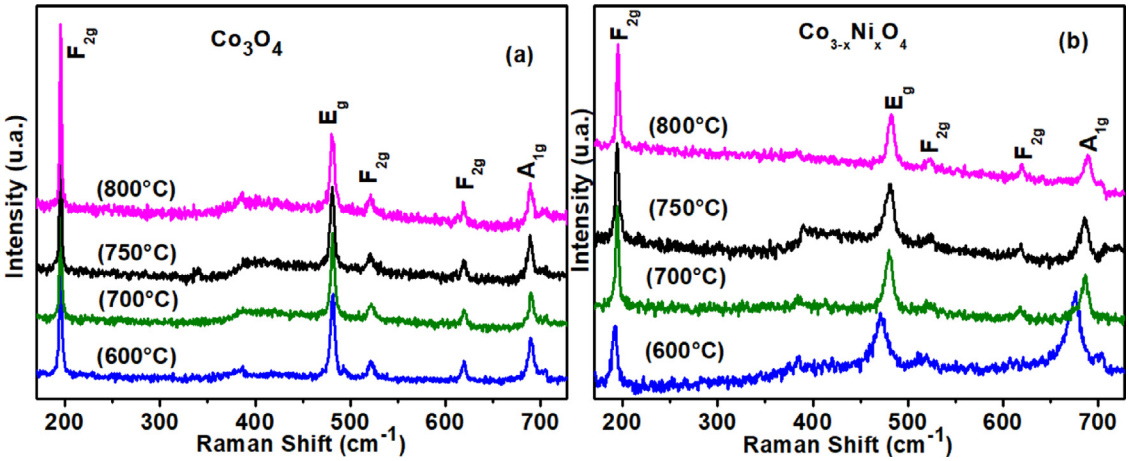

Fig. 7. Raman spectra of Co_3O_4 samples; (a) Co_3O_4 (b) $Co_{3-x}Ni_xO_4$ x = 4%.

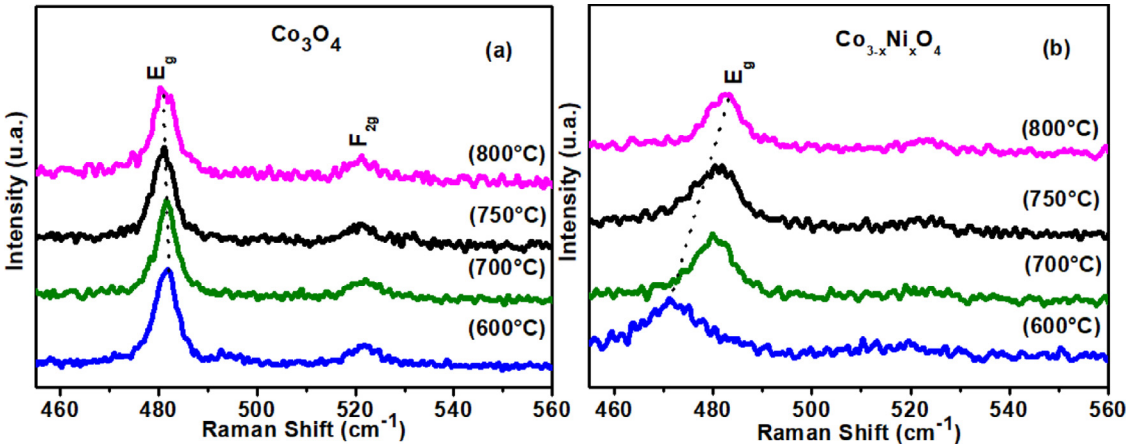

Fig. 8. Raman spectra zoom (a) (b).

very dark samples, it is possible that the laser light absorption process was not negligible and that the local overheating was caused in the samples. Once again, through active Raman modes, it was observed that at 800 °C, there is a change in symmetry for the Ni sample. The peak at 617 cm^{-1} almost disappeared and the spectrum presented broad bands.

The insertion of nickel in the spinel network significantly altered the Raman peaks, by shifting them to higher frequencies as is evident in Fig. 8(a) Co_3O_4, and (b) $Co_{3-x}Ni_xO_4$ [63]. One of the prominent changes can be seen with the mode assigned as A_{1g}, which is induced at the octahedral cation sites by replacing cobalt cations with Ni^{2+}; in this case the band greatly increases its line width. The existence of defects can cause distortion in the crystal lattice as indicated in Fig. 8. Defects or distortion of the network can be better evidenced with Ni-doped samples by Raman shift for low frequencies of the mode around 485 cm^{-1}, as seen in Fig. 8(b). The defects, in fact, are best seen in Raman by increasing the line width of the bands, which is what happens with the A1g mode in the sample with Ni, Fig. 7(b).

The intensity in the Raman peaks is directly associated with increase or decrease of Co^{3+} ions at octahedral sites and the formation of Co^{2+} at the tetrahedral sites [64]. As shown in Table 7, similar values are observed for the active Raman modes of the spinel structure in the Co_3O_4 samples; however, Raman shifts are observed in almost all the vibrational modes in the $Co_{3-x}Ni_xO_4$ samples. For example, mode (A_{g1}) has a 14 cm^{-1} shift, this information can be indicative of the inclusion of the Ni atom in the Co_3O_4 crystal lattice creating defects. The shifting and lengthening of the vibrational modes at 800 °C indicate the start of the CoO phase change. These results confirm the changes evidenced in the x-ray diffractograms of Fig. 6.

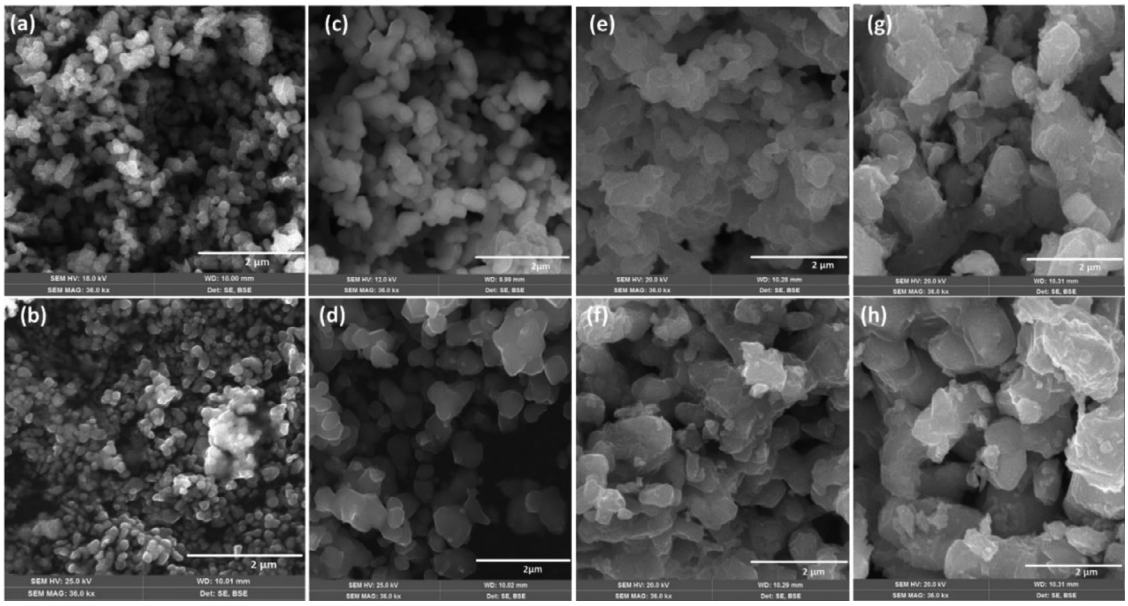

Fig. 9. SEM Images for Co_3O_4 samples at (a) 700 °C, (c) 800 °C, (e) 900 °C, (g) 1000 °C; and $Co_{3-X}Ni_XO_4$ = 4% at (b) 700 °C, (d) 800 °C, (f) 900 °C, (h) 1000 °C.

Table 7
Raman Shift Co_3O_4 and $Co_{3-x}Ni_xO_4$.

Samples	Raman Shift (cm^{-1})				
Co_3O_4	F_{2g}	E_g	$F_{2g(1)}$	$F_{2g(2)}$	A_{g1}
600 °C	195.66	481.67	521.21	619.18	690.26
700 °C	195.75	481.82	521.58	618.90	689.69
750 °C	195.54	481.10	520.87	619.78	689.24
800 °C	195.57	481.19	521.35	619.20	689.48
$Co_{3-x}Ni_xO_4$	F_{2g}	E_g	$F_{2g(1)}$	$F_{2g(2)}$	A_{g1}
600 °C	192.17	471.45	520.63	616.99	676.33
700 °C	194.48	479.85	521.99	617.15	686.78
750 °C	194.61	481.34	522.06	618.98	685.92
800 °C	195.32	482.50	523.02	619.06	689.72

Fig. 9 shows the images of the Co_3O_4 samples exposed to (a) 700 °C, (c) 800 °C, (e) 900 °C and (g) 1000 °C; as well as the $Co_{3-x}Ni_xO_4$, = 4% samples exposed at (b) 700 °C, (d) 800 °C (f) 900 °C and (h)1000 °C. The morphology observed at 700 °C indicates granular formations transformed into nanoplates when the temperature rises to 900 °C and 1000 °C. It is noticed that the insertion of nickel does not substantially change the morphology, but only affects nanoparticle size: it is smaller in the presence of nickel. Li et al., [1] evidenced small pores in the nanoplates which, in turn, provided a large number of edge sites. These SEM results serve as an example, since measurements were collected for all samples, indicating a behavior of increasing particle size with increasing temperature [64]. Regarding the morphology of the samples, they showed a uniform spherical shape and no virtual difference was observed for the material added of Ni in the samples of Co_3O_4. This spherical morphology changes completely at 1000 °C to the plate-like morphology when the structural phase changes.

The nanoparticles obtained at the last calcination temperature (g) and (h) are larger. This is probably due to the excess of thermal energy that was absorbed by the smaller spheres and the interaction between them, generating larger particles with greater agglomeration [65]. As the calcination time and temperature increase, the synthesized particles tend to become larger and more agglomerated, contributing to a change in their plate morphology. According to Jin et al., [66] in hydrothermal synthesis, the morphology of the Co_3O_4 crystal largely depends on the coordination and the pH value of the medium.

4. Conclusions

The compounds Co_3O_4 and $Co_{3-x}Ni_xO_4$ were synthesized by hydrothermal method with heat treatment ranging from 600 to 1000 °C. The results indicated high crystallinity of pure Co_3O_4, as well as with the addition of Ni in the absence of residual phases or phases associated with the addition of nickel when exposed to a temperature equal to or higher than 800 °C. From 900 °C, the transition phase to CoO is observed for both types of samples as a result of the calcination temperatures. SEM analyzes indicate good homogeneity of the nanoparticle. No significant change in morphology is evident in the presence of Ni. However, as the spinel phase change from Co_3O_4 to CoO, its morphology changes from spherical to agglomerated plates at high temperatures. The structural analysis of both types of samples by Rietveld refinement of the experimental XRD showed an increase in the lattice parameter of the centered cubic structure that belongs to the space group *F-43 m* with $a = b = c$ of Co_3O_4 of 8.08551 Å and for $Co_{3-x}Ni_xO_4$ - 8.09276 Å at 800 °C. There is also an increase in the volume of the unit cell with an average value of 528.304 Å for Co_3O_4 and 529.15 Å for nickel-doped Co_3O_4. These variations are associated with cationic defects at tetrahedral and octahedral sites in the Co_3O_4 spinel structure. Through the Scheerr equation, it was observed that the crystallite size reached maximum values of 79.73 nm and 76.8 nm when the samples of Co_3O_4 and $Co_{3-x}Ni_xO_4$ were exposed to 800 °C, respectively, presenting slightly smaller sizes for those nickel-doped samples. This indicates that the addition of nickel to the material not only improves its physical and chemical properties, but also favors the decrease in the size of the crystallite. Likewise, Raman spectroscopy measurements contributed to determine that, given the crystal lattice defects and distortions, the active Raman modes shift and widen their Raman bands, especially for nickel-doped samples. These changes in the calcination temperature spectra of the samples are also attributed to the grain size of the Co_3O_4 structure, formation of oxygen and cobalt vacancies, and the onset of the structural phase change to CoO.

Declaration of Competing Interest

The authors declare that they have no known competing financial interests or personal relationships that could have appeared to influence the work reported in this paper.

Acknowledgments

The authors thank the Universidad Nacional de Colombia-Bogotá, Universidade Federal do Ceará -Fortaleza -Brazil, Professor Angela Raba and Embrapa -Instrumentação, XV de Novembro St., 1452, 13560-970 São Carlos.

References

[1] S. Li, K. Wu. L. Li, L. Suo, Y. Zhu, An architecture of dandelion-type Ni-Co_3O_4 microspheres on carbon nanotube films toward an efficient catalyst for oxygen reduction in zinc-air batteries, Appl. Surf. Sci. 481 (2019) 40–51.
[2] L. Li, Q. Xu, Y. Zhang, J. Li, J. Fang, Y. Dai, X. Li, Low Ni-doped Co_3O_4 porous nanoplates for enhanced hydrogen and oxygen evolution reaction, J. Alloys Compd. 823 (2020) 153750.
[3] S. Dissanayake, N. Wasalathanthri, A.S. Amin, J. He, S. Poges, D. Rathnayake, S. Suib, Mesoporous Co_3O_4 catalysts for VOC elimination: oxidation of 2-propanol, Appl. Catal. 590 (2020) 117366.
[4] Y. Liu, J. Xie, M. Luo, S. Jian, B. Peng, L. Deng, The synthesis and characterization of Al/Co_3O_4 magnetic composite pigments with low infrared emissivity and low lightness, Infrared Phys. Technol. 83 (2017) 88–93.
[5] X. Wang, W. Tian, T. Zhai, C. Zhi, Y. Bando, D. Golberg, Cobalt (II, III) oxide hollow structures: fabrication, properties and applications, J. Mater. Chem. 22 (2012) 23310–23326.
[6] K. Cvejin, M. Śliwa, L. Manjakkal, J. Kulawik, G. Stojanović, D. Szwagierczak, Impedancemetric NO sensor based on YSZ/perovskite neodymium cobaltite operating at high temperatures, Sens. Actuators. 228 (2016) 612–624.
[7] A.S. Vijayanandan, R.S.K. Valappil, R.M. Balakrishnan, Evaluation of photothermal properties for absorption of solar energy by Co_3O_4 nanofluids synthesized using endophytic fungus Aspergillus nidulans, Sustain. Energy Technol. 37 (2020) 100598.
[8] J.C. Medina, S.E.E. Rodil, Zanella, Synthesis of a CeO_2/Co_3O_4 catalyst with a remarkable performance for the soot oxidation reaction, *R. Catal. Sci. Technol.* 10 (2020) 853–863.
[9] A. Numan, M. Khalid, S. Ramesh, K. Ramesh, E.M. Shamsudin, Y. Zhan, P. Jagadesh, Facile sonochemical synthesis of 2D porous Co_3O_4 nanoflake for supercapattery, J. Alloys Compd. 819 (2020) 153019.
[10] W.L. Jia, J. Li, Z.J. Lu, Y.F. Juan, Y. Jiang Q, ynthesis of porous Co_3O_4/Reduced graphene oxide by a two-step method for supercapacitors with excellent electrochemical performance, J. Alloys Compd. 815 (2020) 152373.
[11] A.T. Khalil, M. Ovais, I.I. Ullah, M. Ali, Z.K. Shinwari, M. Maaza, Physical properties, biological applications and biocompatibility studies on biosynthesized single phase cobalt oxide (Co_3O_4) nanoparticles via Sageretia thea (Osbeck.), Arab. J. Chem. 13 (2020) 606–619.
[12] F. Xu, H. Yan, J. Chen, Z. Zhang, C. Fan, Nanoscale Co_3O_4 powders prepared by an enhanced solid-state reaction method, Ceram. Int. 46 (2020) 13893–13899.
[13] M. Zhou, L. Cai, M. Bajdich, M. García-Melchor, H. Li, J. He, X. Zheng, Enhancing catalytic CO oxidation over Co_3O_4 nanowires by substituting Co2+ with Cu2+, ACS Catal. 5 (2015) 4485–4491.
[14] J. Liu, J. Zhang, T. Zhou, S. Wei, Kinetics of reduction of Co_3O_4 by hydrogen, Acta Metall. Sin. 36 (2000) 837–841.
[15] M.A. Abreu-Sepulveda, C. Dhital, A. Huq, L. Li, C.A. Bridges, M.P. Paranthaman, A. Manivannan, The influence of Fe substitution in lanthanum calcium cobalt oxide on the oxygen evolution reaction in alkaline media, J. Electrochem. 163 (2016) F1124.
[16] X. Wang, A. Hu, C. Meng, C. Wu, S. Yang, X. Hong, Recent advance in Co_3O_4 and Co_3O_4-containing electrode materials for high-performance supercapacitors, Molecules 25 (2020) 269.
[17] M. Casas-Cabanas, G. Binotto, D. Larcher, A. Lecup, V. Giordani, J.M. Tarascon, Defect chemistry and catalytic activity of nanosized Co_3O_4, Chem. Mater. 21 (2009) 1939–1947.
[18] S. Li, K. Wu, L. Li, L. Suo, Y. Zhu, An architecture of dandelion-type Ni- Co_3O_4 microspheres on carbon nanotube films toward an efficient catalyst for oxygen reduction in zinc-air batteries, Appl. Surf. Sci. 481 (2019) 40–51.
[19] J. Gao, B. Jiang, C. Ni, Y. Qi, X. Bi, Enhanced reduction of nitrate by noble metal-free electrocatalysis on P doped three-dimensional Co_3O_4 cathode: mechanism exploration from both experimental and DFT studies, Chem. Eng. J. 382 (2020) 123034.
[20] A.L. Kozlovskiy, I.E. Kenzhina, M.V. Zdorovets, FeCo–Fe_2CoO_4/Co_3O_4 nanocomposites: phase transformations as a result of thermal annealing and practical application in catalysis, Ceram. Int. 46 (2020) 10262–10269.
[21] M.V. Zdorovets, A.E. Shumskaya, A.L. Kozlovskiy, Investigation of the effect of phase transformations on the magnetic and electrical properties of Co/Co_3O_4 nanowires, J. Magn. Magn. Mater. 497 (2020) 166079.
[22] P. Cheng, F. Dang, Y. Wang, J. Gao, L. Xu, C. Wang, B. Liu, Gas sensor towards n-butanol at low temperature detection: hierarchical flower-like Ni-doped Co_3O_4 based on solvent-dependent synthesis, Sens. Actuators B Chem. 328 (2021) 129028.
[23] T. Kou, S. Wang, J.L. Hauser, M. Chen, S.R. Oliver, Y. Ye, Y. Li, Ni foam-supported Fe-doped β-Ni (OH) 2 nanosheets show ultralow overpotential for oxygen evolution reaction, ACS Energy Lett. 4 (3) (2019) 622–628.
[24] L. Li, Q. Xu, Y. Zhang, J. Li, J. Fang, Y. Dai, X. Li, Low Ni-doped Co3O4 porous nanoplates for enhanced hydrogen and oxygen evolution reaction, J. Alloys Compd. 823 (2021) 153750.
[25] H. Du, W. Pu, C. Yang, Morphology control of Co_3O_4 with nickel incorporation for highly efficient oxygen evolution reaction, Appl. Surf. Sci. 541 (2021) 148221.
[26] A. Sivakumar, S. Soundarya, S.S. Jude Dhas, K.K. Bharathi, S.M. Dhas, Shock wave driven solid state phase transformation of Co3O4 to CoO nanoparticles, J. Phys. Chem. C 124 (19) (2020) 10755–10763.
[27] A. Pan, Y. Wang, W. Xu, Z. Nie, S. Liang, Z. Nie, J.G. Zhang, High-performance anode based on porous Co_3O_4 nanodiscs, J. Power Source. 255 (2014) 125–129.
[28] J. Cao, S. Wang, H. Zhang, T. Zhang, Constructing one dimensional Co_3O_4 hierarchical nanofibers as efficient sensing materials for rapid acetone gas detection, J. Alloys Compd. 799 (2019) 513–520.
[29] A. Singhal, A. Bisht, A. Kumar, S. Sharma, One pot, rapid synthesis of Co_3O_4 by solution combustion method and its electrochemical properties in different electrolytes, J. Electroanal. Chem. 776 (2016) 152–161.
[30] L. Cardenas, A. Raba, M. Rincon, Synthesis and evaluation of nickel doped Co_3O_4 produced through hydrothermal technique, Dyna (Medellin) 87 (2020) 184–191.
[31] Y.W. Hong, Y.B. Kim, J.H. Paik, J.H. Cho, Y.H. Jeong, J.S. Yun, W.I. Park, Liquid Phase Sintering and Electrical Properties of ZnO-Zn 2 $BiVO_6$- Co_3O_4 Ceramics, J. Korean Inst. Electr. Electron. Mater. Eng. 30 (2017) 74–80.
[32] S. Mehmood, Synthesis and Characterizations of Co_3O_4 Based Nanocomposite for Electrochemical Sensor Applications, University of Malaya, 2018 PhD Thesis.
[33] Y.S. Kim, C.W. Yi, H.S. Choi, K. Kim, Modification of Ni-based cathode material for molten carbonate fuel cells using Co_3O_4, J. Power Sources. 196 (2011) 1886–1893.
[34] Q. Zhao, L. Fu, D. Jiang, J. Ouyang, Y. Hu, H. Yang, Y. Xi, Nanoclay-modulated oxygen vacancies of metal oxide, Commun. Chem. 2 (2019) 1–10.
[35] G. Huang, P. Lou, G.H. Xu, X. Zhang, J. Liang, H. Liu, S. Cheng, Co_3O_4 nanosheet decorated nickel foams as advanced lithium host skeletons for dendrite-free lithium metal anode, J. Alloys Compd. 817 (2020) 152753.
[36] P.B. Koli, K.H. Kapadnis, U.G. Deshpande, M.R. Patil, Fabrication and characterization of pure and modified Co_3O_4 nanocatalyst and their application for photocatalytic degradation of eosine blue dye: a comparative study, J. Nanostruct. Chem. 8 (2018) 453–463.
[37] A. Koneru, Non-Equilibrium Green's Function Based Calculations of Spin Voltage in Cobalt Based Spinel Oxides, PhD Theses West Virginia Univesrity, 2017.
[38] L.G. Liu, W.A. Bassett, T. Takahashi, Isothermal compressions of a spinel phase of Co_2SiO_4 and magnesian ilmenite, J. Geophys. Res. 79 (1974) 1171–1174.
[39] B. Antic, D. Rodic, R. Tellgren, H. Rundlof, Neutron diffraction study of the magnetic and structure properties of $Co_{2.50}Sb_{0.50}O_4$ spinel, J. Magn. Magn. Mater. 219 (1) (2000) 41–44.
[40] T.A. Ferreira, J.C. Waerenborgh, M.H. Mendonça, M.R. Nunes, F.M. Costa, Structural and morphological characterization of $FeCo_2O_4$ and $CoFe_2O_4$spinels prepared by a coprecipitation method, Solid State Sci. 5 (2) (2003) 383–392.
[41] A. Sazonov, M. Meven, V. Hutanu, V. Kaiser, G. Heger, D. Trots, M. Merz, Structural behaviour of synthetic Co_2SiO_4 at low temperatures, Acta Crystallogr. Sect. B. 64 (2008) 661–668.
[42] I.P. Muthuselvam, R.N. Bhowmik, Structural phase stability and magnetism in Co_2FeO_4 spinel oxide, Solid State Sci. 11 (2009) 719–725.
[43] C. Mu, J. Mao, J.Q. Guo, Z. Li, W. Qin, S.Z. Qiao, Rational design of spinel cobalt vanadate oxide Co_2VO_4 for superior electrocatalysis, Adv. Mater. 32 (2020) 1907168.
[44] Q. Tang, R. Dieckmann, Floating-zone growth and characterization of single crystals of cobalt orthosilicate, Co_2SiO_4, J. Cryst. Growth 317 (2011) 119–127.
[45] S. Hosoya, H. Takei, Growth of Co_2SiO_4 by the floating-zone method, J. Jpn. Assoc. Cryst. Growth. 5 (1978) 101.
[46] G. Subías, V. Cuartero, J. García, J. Blasco, S. Lafuerza, S. Pascarelli, G. Garbarino, Investigation of pressure-induced magnetic transitions in $Co_xFe_{3-x}O_4$ spinels, Phys. Rev. B Condens. Matter. 87 (2013) 094408.
[47] D. Bauer, T.E. Ashton, A.R. Groves, A. Dey, S. Krishnamurthy, N. Matsumi, J. Darr, A, continuous hydrothermal synthesis of metal germanates (M_2GeO_4; M= Co, Mn, Zn) for high-capacity negative electrodes in Li-ion batteries, Energy Technol. 8 (2020) 1900692.
[48] Y. Feng, J. Liu, D. Wu, Z. Zhou, Y. Deng, T. Zhang, K. Shih, Efficient degradation of sulfamethazine with $CuCo_2O_4$ spinel nanocatalysts for peroxymonosulfate activation, Open Chem. Eng. J. 280 (2015) 514–524.
[49] N.H. Perry, T.O. Mason, C. Ma, A. Navrotsky, Y. Shi, J.S. Bettinger, A. Zunger, Co_3O_4–Co_2ZnO_4 spinels: the case for a solid solution, J. Solid State Chem. 190 (2012) 143–149.
[50] D. Mohanty, H. Gabrisch, Comparison of magnetic properties in Li_xCoO_2 and its decomposition products $LiCo_2O_4$ and Co_3O_4, Solid State Ion 194 (2011) 41–45.
[51] J. Xiong, S. Mo, L. Song, M. Fu, P. Chen, J. Wu, D. Ye, he effect of existence states of PdOx supported by Co_3O_4 nanoplatelets on catalytic oxidation of methane, *Appl. Catal. A* 598 (2020) 117571.
[52] A. Zakutayev, T.R. Paudel, P.F. Ndione, J.D. Perkins, S. Lany, A. Zunger, D.S. Ginley, Cation off-stoichiometry leads to high p-type conductivity and enhanced transparency in Co_2ZnO_4 and Co_2NiO_4 thin films, Phys. Rev. B: Condens. Matter. 85 (2012) 085204.
[53] X. Tong, Z. Hai, D. Cui, L. Gao, Q. Zhang, H. Xu, J. Liu, Investigation of lattice distortion of Co_3O_4 nanoparticles prepared by a carbon-assisted method, Microelectron. Eng. 159 (2016) 17–20.
[54] H. Du, W. Pu, C. Yang, Morphology control of Co_3O_4 with nickel incorporation for highly efficient oxygen evolution reaction, Appl. Surf. Sci 541 (2021) 148221.
[55] X. Xie, C. Ni, Z. Lin, D. Wu, X. Sun, Y. Zhang, W. Du, Phase and morphology evolution of high dielectric CoO/Co3O4 particles with Co_3O_4 nanoneedles on surface for excellent microwave absorption application, Chem. Eng. J. (2020) 125205.
[56] J.A.K. Tareen, A. Małecki, J.P. Doumerc, J.C. Launay, P. Dordor, M. Pouchard, P. Hagenmuller, Growth and electrical properties of pure and Ni-doped Co_3O_4 single crystals, Mater. Res. Bull. 19 (1984) 989–997.
[57] S. Kuboon, Y.H. Hu, Study of NiO– CoO and Co_3O_4– Ni_3O_4 solid solutions in multiphase Ni– Co– O systems, Ind. Eng. Chem. Res. 50 (2011) 2015–2020.

[58] A. Sivakumar, S. Soundarya, S.S. Jude Dhas, K.K. Bharathi, S.M.B. Dhas, Shock wave driven solid state phase transformation of Co_3O_4 to CoO nanoparticles, *J. Phys. Chem. C* 124 (2020) 10755–10763.
[59] G.A. El-Shobaky, M.A. Shouman, S. El-Khouly, effect of silver oxide doping on surface and catalytic properties of Co3O4/Al2O3 system, M. Mater. Lett. 58 (2004) 184–190.
[60] L.J. Cardenas-Flechas, A.M. Raba, J. Barba-Ortega, L.C. Moreno, M.R. Joya, Effect of calcination temperature on the behavior of the agglomerated Co3O4 nanoparticles obtained through the sol–gel method, J. Inorg. Organomet. Polym. 31 (2021) 121–128.
[61] M.T. Makhlouf, B.M. Abu-Zied, T.H. Mansoure, Effect of calcination temperature on the H_2O_2 decomposition activity of nano-crystalline Co_3O_4 prepared by combustion method, J. Nanopart. Res. 274 (2013) 45–52.
[62] S.W. Oh, H.J. Bang, Y.C. Bae, Y.K. Sun, Effect of calcination temperature on morphology, crystallinity and electrochemical properties of nano-crystalline metal oxides (Co_3O_4, CuO, and NiO) prepared via ultrasonic spray pyrolysis, J. Power Sources 173 (2007) 502–509.
[63] S. Mo, H. He, Q. Ren, S. Li, W. Zhang, M. Fu, D. Ye, Macroporous Ni foam-supported Co_3O_4 nanobrush and nanomace hybrid arrays for high-efficiency CO oxidation, J. Environ. Sci. 75 (2019) 136–144.
[64] P. Sennu, H.S. Park, K.U. Park, V. Aravindan, K.S. Nahm, Y.S. Lee, Formation of NiCo2O4 rods over Co_3O_4 nanosheets as efficient catalyst for Li–O2 batteries and water splitting, J. Catal. 349 (2017) 175–182.
[65] G. A.Babu, G. Ravi, Y. Hayakawa, M. Kumaresavanji, Synthesis and calcinations effects on size analysis of Co_3O_4 nanospheres and their superparamagnetic behaviors, J. Magn. Magn. Mater 375 (2015) 184–193.
[66] L. Jin, X. Li, H. Ming, H. Wang, Z. Jia, Y. Fu, J. Zheng, Hydrothermal synthesis of $Co_3O_4$with different morphologies towards efficient Li-ion storage, RSC Adv. 4 (2014) 6083–6089.